J. Fluid Mech. (1984), *vol.* 142, *pp.* 97–120
Printed in Great Britain

On the use of an annulus to study mixed-layer entrainment

By J. W. DEARDORFF AND S.-C. YOON
Department of Atmospheric Sciences, Oregon State University, Corvallis, Oregon 97331

(Received 14 June 1983 and in revised form 3 January 1984)

An annulus covered by a rotating screen (or surface) which imparts stress and turbulence to the upper of two fluid layers has been shown by Scranton & Lindberg (1983) and Jones & Mulhearn (1983) to produce mixed-layer entrainment that is dependent on annulus curvature and geometry. This general result is confirmed here, where photographs of the mixed-layer interface indicate that turbulent entrainment rapidly diminishes away from the outer wall. The problem is explained as a damping of the turbulence within the bulk of the mixed layer by inertial stability associated with angular momentum increasing rapidly with radius except very close to the outer wall. Through hot-film-anemometer measurements, a shallow turbulent Ekman layer is found to exist immediately underneath the rotating screen, having a depth of order $0.4u_* r/\bar{v}$, where u_* is the friction velocity, $\bar{v}$ is the mean circumferential flow speed within the layer and r is the radius. For r of order 1 m, this depth is typically only a small fraction of the mixed-layer depth determined from the density profile.

When the stress input is placed near the inner wall, the mean-flow radial profile is much more nearly irrotational and the turbulence-damping problem becomes minimal. The entrainment is then much more uniform with radius, and local interfacial scaling can be used to relate the entrainment rate to one or more local Richardson numbers containing a turbulent velocity scale rather than u_* or $\Delta\bar{v}$, where Δ signifies the change across the interface. Although u_* and $\Delta\bar{v}$ are proper 'external' scales for entrainment in a horizontally homogeneous mixed layer that is turbulent throughout, a local internal turbulent velocity scale can alternatively be used. Entrainment rates thus scaled are presented and compared with Turner's (1973) locally scaled entrainment.

1. Introduction

The rate of growth of a turbulent mixed layer has received much study in the past decade because it helps determine the mean thickness $\bar{h}$ reached by an atmospheric or oceanic mixed layer at any given time. Laboratory studies of this topic are appealing because grave uncertainties involved in geophysical studies can be eliminated or alleviated. The chief uncertainty is the mean vertical motion at the outer edge of the boundary layer and horizontal divergence within, which can cause changes in mixed-layer depth exceeding that due to entrainment on short timescales. In the atmosphere the vertical motion is associated with large-scale weather systems or with mesoscale disturbances; in ocean mixed layers it is associated with internal waves or upwelling. On larger timescales the governing conditions often vary too much outside the laboratory for useful time-averaged measurements to be obtained.

The primary laboratory apparatus for exploring mixed-layer entrainment has been the annulus containing water with a rotating screen at its top through which momentum is continuously imparted to the mixed layer beneath (Kato & Phillips 1969; Kantha, Phillips & Azad 1977). Their annulus had an outer diameter of 1.52 m and an annulus gap width W of 0.23 m. The annular geometry eliminates unwanted end effects present in a linear channel whose length may not be great enough for equilibrium conditions to be attained. Also, it apparently enables simulation of a horizontally homogeneous mixed layer whose depth varies only with time and not in space. In the study of Kato & Phillips (1969) the annulus fluid was stably stratified initially, using salt, and subsequent imposition of momentum flux by the rotating screen caused a deepening of the upper, less-dense fluid layer.

An even simpler initial condition is the two-layer system treated by Kantha *et al.* (1977) in which an upper layer of fresh water initially lies above a salty layer of greater, uniform density. After the experiment commences and entrainment proceeds, the upper layer again gradually deepens and becomes salty, through entrainment at the rate w_e. In either type of experiment, the magnitude of the density jump $\Delta\rho$ across the outer edge of the mixed layer appears to be the proper measure of stratification (or more precisely $g\,\Delta\rho/\bar{\rho}$ in the ocean and $g\,\Delta\theta/\bar{\theta}$ in the atmosphere, where g is the gravitational acceleration, θ is virtual potential temperature and the overbar represents a mean).

Results from these two laboratory studies were analysed by normalizing w_e by the friction velocity u_*, and presented as a function of a stress Richardson number R_τ given by

$$R_\tau = \frac{g\,\Delta\rho}{\bar{\rho}}\frac{\bar{h}}{u_*^2}, \tag{1}$$

where h is the mixed-layer depth. The greater R_τ was, the smaller w_e/u_* was found to be, with more rapid entrainment occurring in the two-layer system, all other measured quantities being the same. A parameterization of the Kato & Phillips (1969) results has been particularly useful to oceanographers in predicting mixed-layer temperature (see e.g. Denman & Miyake 1973; Niiler & Kraus 1977).

In a later study of the two-layer system by Kantha (1978), an annulus was used of only half the size of the previous one. Significantly smaller values of w_e/u_* were obtained for given values of R_τ in comparison with the results of Kantha *et al.* (1977). These results began to raise some questions on the validity of the annular geometry in simulating rectilinear mean geophysical flows, and/or of the scaling laws used.

The latter question was addressed by Deardorff & Willis (1982) using an annulus of outer diameter 1.18 m and gap width $W = 0.18$ m. They found intermediate w_e/u_* values as a function of R_τ, but also found that an additional parameter R_v (in the notation of Price 1979) is very important:

$$R_v = \frac{g\,\Delta\rho}{\bar{\rho}}\frac{\bar{h}}{(\Delta V)^2}, \tag{2}$$

where ΔV is the difference in speed across the mean density interface (which has a finite thickness based on averaged properties). The quantity ΔV was found to be significantly smaller than the mean mixed-layer flow speed $\bar{v}$, owing to viscous propagation of momentum beyond the mixed-layer interface, when w_e was not too large. Their main result was the entrainment relationship

$$\frac{w_e}{\Delta V} = 0.47 R_\tau^{-1} R_v^{-0.9} \tag{3}$$

for R_τ, R_v based on interface-centred $\bar{h}$-values. The -1 power-law dependence for R_τ was adopted from theoretical considerations of Price (1979) and Thompson (1979).

In finding that both u_* and ΔV were important in increasing w_e, this study had apparently bridged the gap between earlier studies in which only ΔV was utilized as the velocity scale (Ellison & Turner 1959; Lofquist 1960; Moore & Long 1971) and the annulus studies in which only u_* was utilized. The smaller entrainment rate found for the smaller annulus of Kantha was then explainable as a result of smaller ΔV values, for a given u_*, associated with relatively greater sidewall drag in the smaller apparatus with smaller W.

Both Kantha (1978) and Deardorff & Willis (1982) noted that a substantial mean interfacial tilt can occur, such that $\bar{h}$ increases with increasing radius, especially when R_v is small. The larger the annulus, the smaller the R_v values that can be tolerated before horizontal entrainment across the tilting interface becomes too large a fraction of vertical entrainment. Since horizontal entrainment is unopposed by vertical stability, the effect could be undesirably large unless the mean interfacial slope is less than perhaps 0.1.

A key experimental study by Scranton & Lindberg (1983) emphasized several additional deficiencies stemming from the use of the annular geometry. First, it was noted that a secondary circulation coexists with the circumferential flow, directed away (downwards) from the rotating screen at the outer wall and towards it at the inner wall of the annulus. Secondly, the level of turbulence in the mixed layer near the interface was found to be much smaller in the inner 85% or so of the annulus than in the outer 15%. Significant interfacial tilts were also noticed. The implications for the entrainment rate are that: (*a*) a spurious entrainment may be occurring from the secondary circulation carrying fluid of intermediate density inwards along the interface and thence into the mixed layer near the inner wall where a wedge of nearly stagnant fluid had been observed; and (*b*) *bona fide* turbulent entrainment decreases so much with decreasing radius that its average value across the annulus (which is the measured w_e) is unlikely to be the same as would occur in a rectilinear or geophysical system, holding other conditions the same.

Results from a study by Jones & Mulhearn (1983), with an annulus about twice the size of the one used by Kato & Phillips, are not inconsistent with the findings of Scranton & Lindberg. With the larger annulus it was found that w_e correlated best with Richardson numbers containing the gap width W instead of $\bar{h}$. A good approximation to the Jones & Mulhearn results on entrainment rate is

$$\frac{w_e}{\Delta V} = 0.7\left(\frac{\bar{h}}{W}\right)^2\left(\frac{\bar{v}}{\Delta V}\right)^3 R_\tau^{-1} R_v^{-1}, \tag{4}$$

in which results from previous two-layer annulus systems were included by estimating $u_*/\bar{v}$ knowing the screen drag coefficient. Their result is fairly close to (3), considering that in Deardorff & Willis' study $\bar{h}/W$ averaged 0.67, $\bar{v}/\Delta V$ averaged about 1.45 and R_v averaged about 3. However, the studies of Scranton & Lindberg and Jones & Mulhearn raised serious doubts that (3) or (4) has any geophysical significance.

Therefore the purposes of the present study are: (*a*) to document further the deficiencies of the conventional annulus with rotating screen for investigating mixed-layer entrainment; (*b*) to explore reasons why the turbulence and entrainment within the conventional annulus may depend on radius and gap width; and (*c*) to propose improvements to the annulus stress-input configuration which greatly ameliorate the deficiencies, provided that the interfacial tilt is not too large.

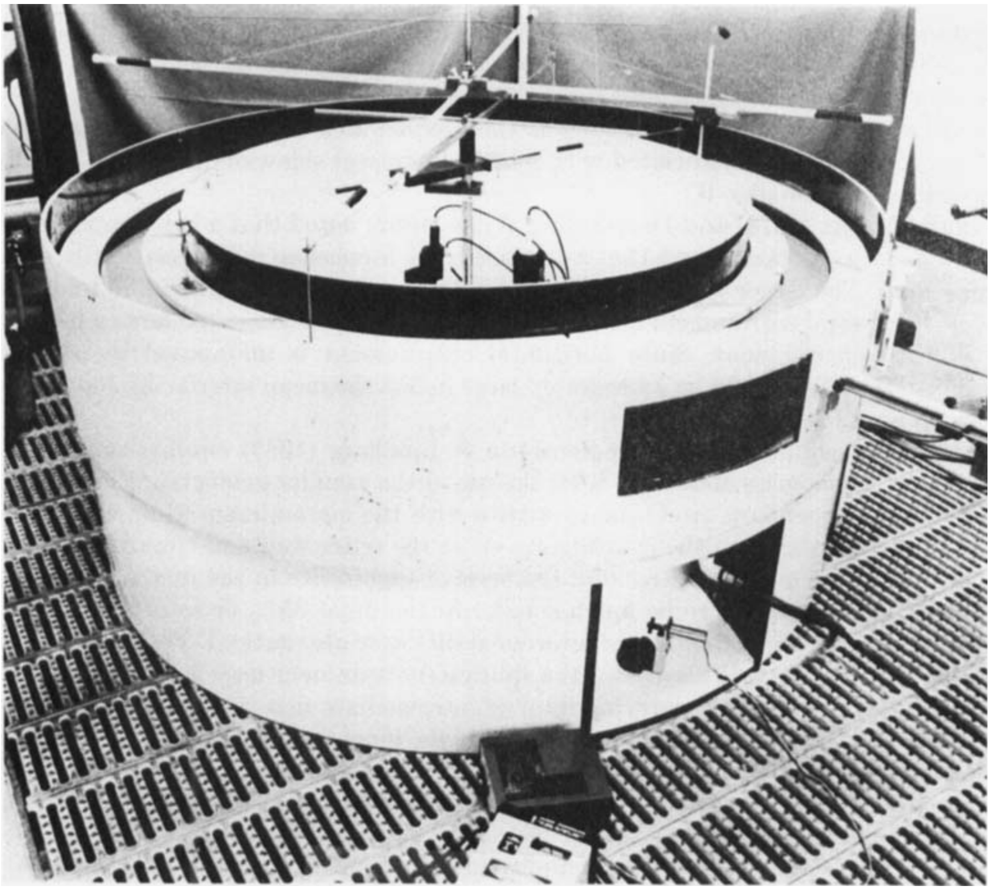

FIGURE 1. The annulus at Oregon State University, Department of Atmospheric Science, showing inner and outer sections of rotatable screen floating on the water surface. Photography of the density interface with dye in the mixed layer was accomplished through the rectangular window (right front) with illumination from below via the small rotatable mirror shown. Horizontal traverses with the hot-film anemometer were made through the port just to the right of this window. The vertically traversing laser for obtaining mixed-layer depths, and the vertically traversing density probe (scarcely visible) are located farther around the annulus to the right.

2. The present annulus and equipment

This annulus, shown in figure 1, is made of fibreglass cylinders with an outer diameter of 2.00 m and a gap of 0.30 m. Its rotating screen floats on the water surface to facilitate the stress measurements and is made of rigid plastic foam with a smooth underside. However, this 'screen' is unconventional in being split into one or more of three sections, each covering about 30 % of the annulus surface area. The three sections could be rotated independently, although usually the outer two sections either were caused to rotate rigidly with the inner one, or were lifted off the water surface. The screen drive motors, located near the centre of the annulus, provided rotation through a central triaxial shaft. Horizontal drive arms extending out from this shaft contained sets of strain gauges for measuring the torques exerted against the respective screens. The torque applied to each screen could be measured separately. The sum of their torques, when divided by the mean radius $\bar{r}$ and the total annulus area, gave the average stress $\tau = \rho u_*^2$. The strain-gauge signals were linear with torque and their calibration straightforward.

The total water depth in the annulus was about 0.3 m. The depth of the upper, less-dense water layer initially ranged from about 0.04 to 0.07 m, with saltier water (using NaCl rock salt) occupying the remaining depth. The water was filtered and degassed before adding any salt.

The annulus has two sidewall viewing windows, one of which is visible in figure 1, through which the hot-film anemometer could be inspected for presence of any bubbles. Beneath each annulus side window a large bottom window permits illumination of the mixed-layer density interface for purposes of interfacial-depth measurement or photographic observations.

The constant-temperature hot-film anemometer probe barely visible in the upper right of the front window of figure 1 is of the two-wire V-configuration. The centres of the two wires are separated by about 3 mm; consequently, to avoid significant errors, no measurements were made within 1 cm of a wall or the screen where turbulence scales become smaller. The hot-film output voltages as well as anemometer radial or vertical position were fed into the data acquisition system to be described. The anemometer equation utilized is

$$(E/E_0)^2 = A + B(\rho v_{\mathrm{ef}})^{0.3}, \tag{5}$$

where E is the output voltage, E_0 its zero-speed reference value, A and B are empirical constants, and v_{ef} is the flow speed normal to either sensing wire axis. The directional response was assumed to obey the cosine law. Equation (5) was found to hold down to about 2 cm s^{-1}. The anemometer was usually calibrated in a separate towing tank of dimensions 1.2 m long and 0.3 m wide along which it could be towed steadily at speeds ranging from 0.02 to 0.25 m s^{-1}, and from which the exponent of 0.3 in (5) was obtained. Abbreviated 3-point calibrations were, however, performed shortly before and after each experiment, from which E_0, A and B were determined. For the entrainment experiments to be reported in §6, these calibrations were performed *in situ* along a 0.7 m path within the annulus immediately before and after the experiment so that the anemometer would not have to be removed from the water during the interim and be subjected to extraneous sources of contamination. During an experiment the hot-film anemometer could be positioned either horizontally in successive steps, in which case it measured the circumferential and radial velocity components, or vertically, in which case it measured the circumferential and vertical velocity components. Additional system details may be found in Yoon (1983).

The data-collection system accepted analog input voltages from 17 channels at intervals of 0.05 s, converted them to digits lying between 0 and 4095, and stored these on magnetic tape for subsequent computer analysis and graphic plotting.

To obtain measurements of the mean interfacial height $\bar{h}$ and tilt, $\partial\bar{h}/\partial r$, two vertically directed white-light beams with sources located underneath an annulus bottom window at radii 0.75 m and 0.95 m allowed h to be observed by fluorescing an indicator dye present in the mixed-layer fluid. A horizontally spread laser beam directed in from a side window was then moved vertically until its beam intercepted first one and then the other of the two vertical beams at the interface height where the dye contrast was greatest. The height of the laser was fed into the data acquisition system along with event-marker signals. The mean interface height was taken as the average of values at the two radii, smoothed in time.

The mean interfacial tilt could be obtained to an accuracy of ± 1.5 mm across this radial increment of 0.2 m, provided that the visual delineation of h was clear cut. This tilt was sometimes monitored not only to ensure that its magnitude was not too large to invalidate the experiment, but also to enable an independent estimate of ΔV. Because of the approximate balance between the average centrifugal force in the mixed layer and the radial pressure-gradient force of which the interfacial tilt is a consequence, the relation for ΔV is

$$\Delta V = \bar{v} - \left[\bar{v}^2 - \frac{\bar{r} g \Delta \rho}{\bar{\rho}} \frac{\partial \bar{h}}{\partial r}\right]^{\frac{1}{2}}, \tag{6}$$

where $\bar{v}$ here is the mixed-layer mean tangential velocity centred at the radius $\bar{r} = 0.85$ m. For typical conditions of $\Delta\rho/\bar{\rho} = 0.04$, $\bar{v} = 12$ cm s^{-1}, and a variation in $\bar{h}$ of 0.08 cm over $\Delta r = 0.2$ m, ΔV from (6) is 8.7 cm s^{-1}.

Sideview photographs of the interfacial excursions were obtained by sweeping an argon-laser beam in a vertical plane extending through a bottom window when a small amount of fluorescein dye was present within the mixed layer. Mixed-layer fluid was caused to fluoresce when intercepted by the moving beam. An optical filter allowed only light in the fluorescing wavelength band to be viewed by the camera. Time exposures of about 3 s were required to ensure that the beam sweep had progressed across the entire annulus gap.

Vertical profiles of fluid density were obtained by traversing a conductivity probe vertically at a speed of about 1.2 cm s^{-1}. The horizontally oriented sensor needle, with exposed platinum-wire tip, has a diameter of 0.7 mm, while the larger electrode (stainless-steel probe body) has a diameter of 3.2 mm. Its output voltage is quasi-linear with salinity or density, and a quadratic calibration curve served well. A 3-point calibration was performed before each experiment, with a 2-point *in situ* calibration being performed additionally at the commencement of each experiment. The vertical traversing path was located midway between annulus sidewalls. Although the probe's vertical resolution was found to be better than ± 1 mm and its response time less than 0.03 s, hysteresis effects caused a discrepancy between values from up and down traverses in regions of strong density gradient. This error did not affect the determination of $\Delta\rho$ and Δh (the interfacial thickness), however, and for purposes of comparing results against laser-determined mean h-values, successive up and down traverses of the conductivity probe were averaged together before $\bar{h}$ was estimated.

For results to be described in §3 all three annulus screens were employed in a mode of solid rotation; i.e. in the conventional manner.

3. Deficiencies of the conventional annulus: solid-rotation (SR) mode

3.1. *Structure of the interface*

Representative photos of the interfacial structure for the solid-rotation (SR) mode for $u_* = 0.8$ cm s^{-1} are shown in figure 2. Under these conditions, only the outer 30 % or so of the annulus surface area appears to have a turbulent density interface. The inner region is so non-turbulent that striae of dye would sometimes occur near the interface and persist, making it difficult to define or estimate h in the SR mode.

3.2. *Secondary circulation*

In the SR mode the secondary radial flow component $\bar{u}(r)$, normalized by u_*, is shown in figure 3 for depths $0.9\bar{h}$ and $0.17\bar{h}$, for $u_* = 1.3$ and 0.8 cm s^{-1} respectively. The data include some mean values from tracking plyolite particles of about 1 mm diameter and of approximate density 1.02 g cm^{-3} that were initially located at equilibrium on the density interface (in experiments when the hot-film anemometer

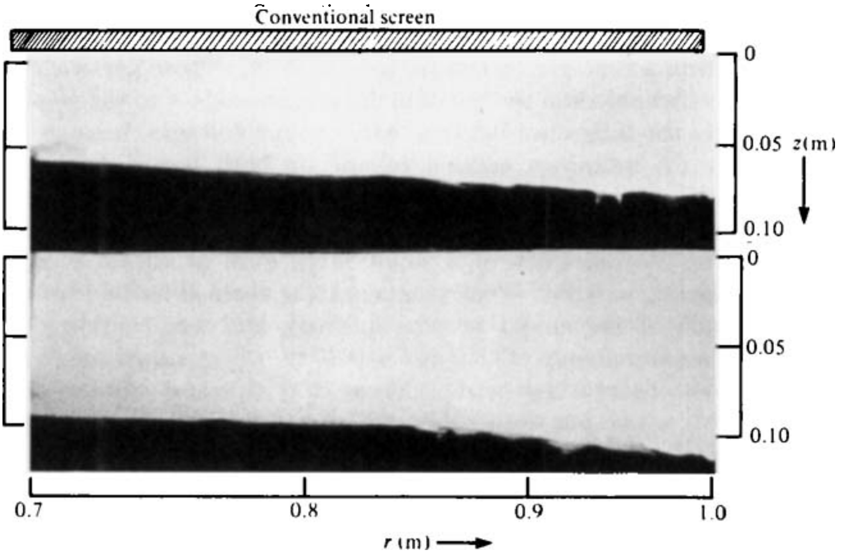

FIGURE 2. Vertical cross-sectional photograph of the mixed layer (upper light region) and denser lower layer for the solid-rotation (SR) mode when (*a*) $\bar{h} = 7$ cm and (*b*) $\bar{h} = 10$ cm. $u_* = 0.8$ cm s^{-1}. Inner wall of annulus is on left and outer wall on right. Interfacial irregularities are invisible only on the right.

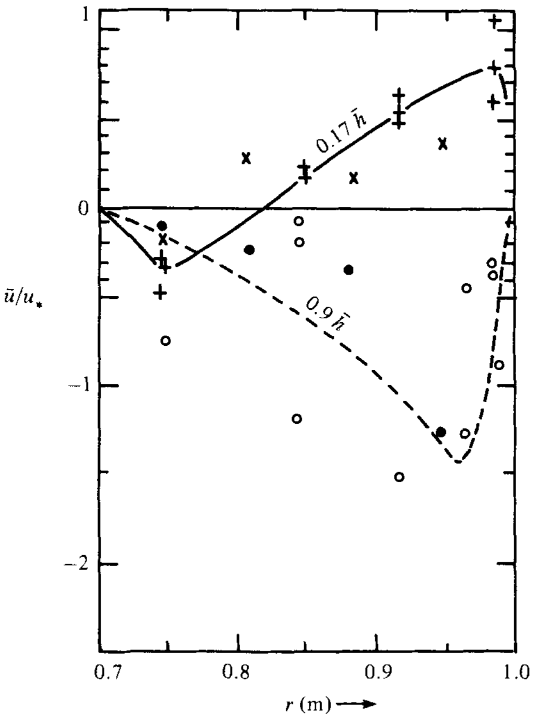

FIGURE 3. Mean radial flow $\bar{u}$, normalized by u_*, for the SR mode as a function of radius and estimated from hot-film anemometer measurements for $z = 0.9\bar{h}$ (○, ----) and for $z = 0.17\bar{h}$ (+, ——). For the former case $u_* = 1.3$ cm s^{-1}; for the latter case $u_* = 0.8$ cm s^{-1}; in both cases $\bar{h} = 6$–9 cm. ●, × are estimates for $z = 0.9\bar{h}$ and $0.17\bar{h}$, respectively, derived from photographic tracking, viewed from below, of neutrally buoyant particles.

was not deployed). After start-up of the experiment, most of these particles drifted inwards, where they collected (and remained) in a wedge-shaped region along the inner wall within a time period comparable to W/u_*. These particle data have more statistical significance than the hot-film data, with respect to the weak $\bar{u}$-component which involves the difference between wire output voltages, because of gradual loss of sensitivity (of unknown causes) of one or both hot-film wires during some experiments. (Only the data for which the value of E_0 changed less than 5 % for each hot wire before and after the experiment are shown in this and subsequent figures.)

Figure 3 implies existence of a single large gyre of width W and strength of magnitude near u_* or $0.05\bar{v}$. Weak compensating vertical motion towards the screen within the bulk of the mixed layer is inferred, and was confirmed from hot-film anemometer measurements of $\bar{w}(z)$ at $r = 0.85$ m, where values averaged $-0.3u_*$ for $z = 0.4\bar{h}$. These observations confirm those of Scranton & Lindberg (1983). One of their inferences which our data support is that some fraction of outer-layer fluid is carried along with the inward-directed branch of the secondary circulation at $z = \bar{h}$ and collects in the wedge-shaped region near the inner wall. There the weak vertical return current of the circulation gradually carries this fluid farther into the mixed layer, and constitutes a laminar entrainment which might exceed the turbulent entrainment occurring near the outer wall (figure 2).

3.3. *Radial profiles of turbulent intensities and $\bar{v}$*

Radial profiles of $\overline{v'^2}$ (circumferential) and $\overline{u'^2}$ (radial) turbulence intensities, relative to u_*^2, are presented in figures 4 and 5 for the SR mode for the same two depths. These variances are associated with individual averaging periods of 13 s. From a study in which much longer period measurements were made with the density interface replaced by a rigid plate, it was noted that the 13 s period contains about 80 % of the total variance. Turbulence intensities to be reported are thus slight underestimates in general. The scatter in the data in these and subsequent figures is relatively large because the averaging period had to be kept small due to the unsteady nature of the problem of mixed-layer growth.

The main feature of figures 4 and 5 is that the turbulence level in the SR mode decreases rapidly away from the outer wall, at the greater depth, in qualitative agreement with the findings of Scranton & Lindberg (1983) and with figure 2. Much closer to the rotating screen, figures 4 and 5 show that this variation is much reduced. However, the turbulence magnitude is 5–10 times smaller than what is expected within or very close to the surface layer of a shear-driven neutral boundary layer in rectilinear flow (Lumley & Panofsky 1964, pp. 146, 155; Comte-Bellot 1965).

Radial profiles of the mean circumferential velocity component $\bar{v}$, multiplied by radius (angular momentum per unit mass) and normalized by mean radius times u_*, are presented in figure 6. At the greater depth the steep increase of angular momentum with increasing r suggests that inertial stability may be acting to damp the turbulence. This possibility will be explored in §4.

3.4. *Vertical profiles*

Measured vertical profiles of $\overline{v'^2}/u_*^2$, $\overline{w'^2}/u_*^2$ and $\overline{v'w'}/u_*^2$ are shown in figures 7 and 8 at $r = 0.85$ m for $u_* = 0.8$ cm s^{-1}. At small z a very rapid decrease of all of these quantities with depth is apparent, with some shear enhancement occurring at the interface $z = \bar{h}$. However, figure 8 in particular demonstrates the complete inability of the annulus to simulate a geophysical shear-driven mixed layer in rectilinear flow within a rotating coordinate system. The dotted curve is the expected stress

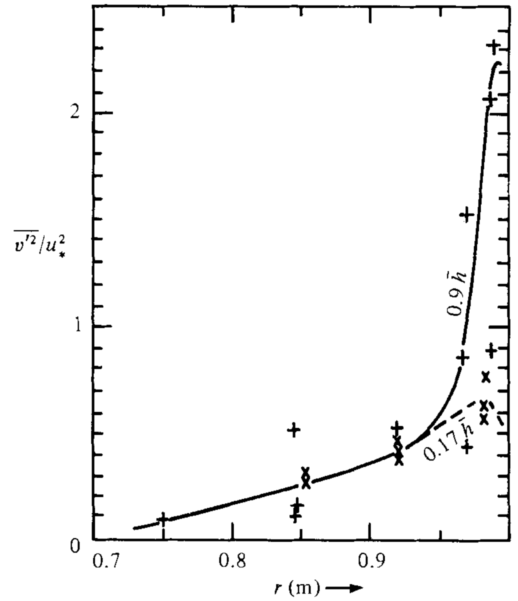

FIGURE 4. Circumferential component of turbulence intensity $\overline{v'^2}$, normalized by u_*^2, for the SR mode as a function of radius for $z = 0.9\bar{h}$ (+, ——) and for $z = 0.17\bar{h}$ (×, – – –). For $u_* = 0.8$ cm s^{-1} and $\bar{h} = 6$–8.5 cm.

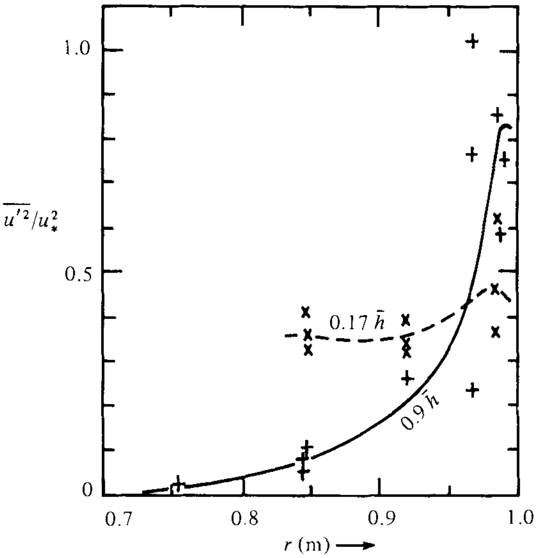

FIGURE 5. Radial component of turbulence intensity $\overline{u'^2}$, normalized by u_*^2, for the SR mode as a function of radius for the two heights. See also figure 4 caption.

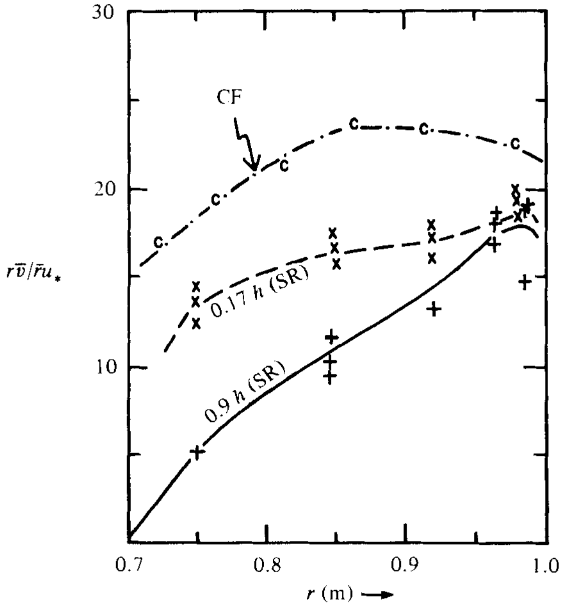

FIGURE 6. Angular momentum $r\bar{v}$, normalized by $\bar{r}u_*$ ($\bar{r} = 0.85$ m) as a function of radius. +, SR mode for $z = 0.9\bar{h}$ for which $\bar{h} = 6$–9 cm and $u_* = 0.8$ and 1.3 cm s^{-1}; ×, SR mode for $z = 0.17\bar{h}$ with $\bar{h} = 6$–7 cm and $u_* = 0.8$ cm s^{-1}; c, CF mode with pairs of data points averaged together, for $z = 0.5\bar{h}$ with $\bar{h} = 6$–7 cm and $u_* = 0.8$ cm s^{-1}.

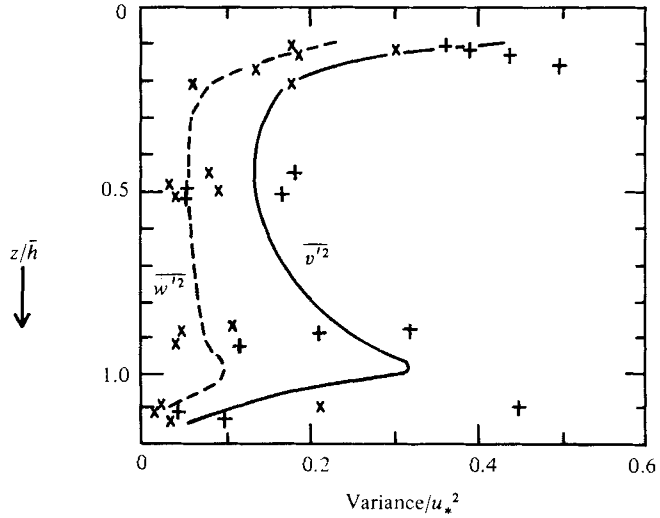

FIGURE 7. Vertical profiles of $\overline{v'^2}/u_*^2$ (+) and $\overline{w'^2}/u_*^2$ (×) for the SR mode at $r = 0.85$ m ($u_* = 0.8$ cm s^{-1}, $\bar{h} = 6$–9 cm).

distribution for that case for a boundary-layer depth of $\bar{h}$ (see e.g. Kundu 1980, figure 10). Below a depth of about $0.4u_*/(\bar{v}/r)$, which is about $0.2\bar{h}$ in our annulus, $\overline{v'w'}$ is completely damped out, and is much smaller than desired even closer to the rotating screen. Subsequent vertical profiles using an X-configuration hot-film anemometer instead of the V-configuration confirmed these results.

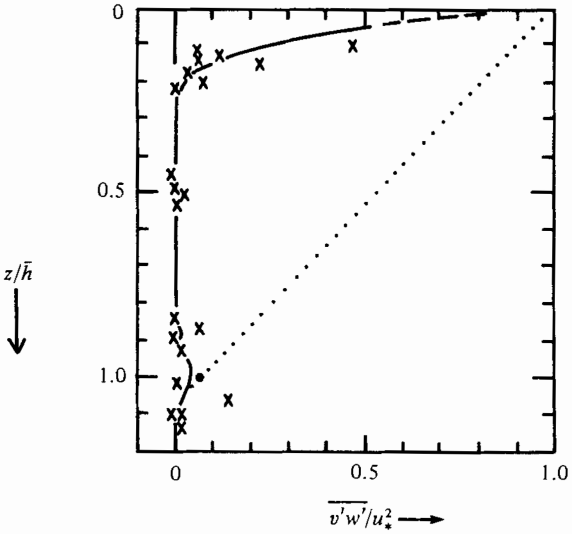

FIGURE 8. Vertical profile of $\overline{v'w'}/u_*^2$ (×) for the SR mode at $r = 0.85$ m. ● at $z/\bar{h} = 1$ is the expected interfacial value using a zero-order jump model with observed values of entrainment and ΔV. (Data are for $u_* = 0.8$ cm s^{-1} and $\bar{h} = 6$–9 cm.) ...., stress distribution to be expected if Ekman layer occupied the entire mixed layer.

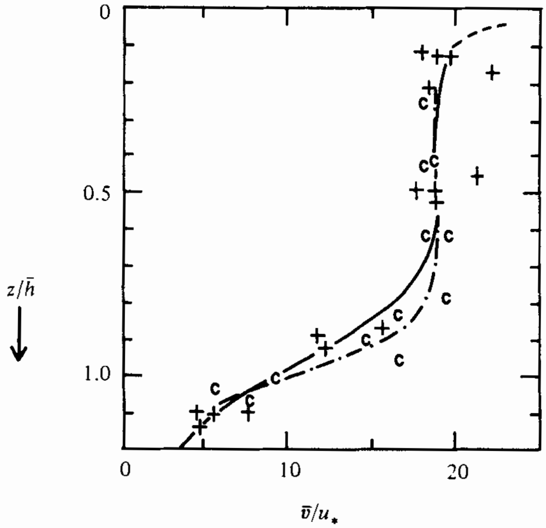

FIGURE 9. Scaled vertical profiles of $\bar{v}/u_*$ for the SR mode (+, ——) for $\bar{h} = 6$–9 cm, and for the CF mode (c, –·–·–·) for $\bar{h} = 8$–12 cm). In both cases $u_* = 0.8$ cm s^{-1}, $r = 0.85$ m.

The vertical profile of $\bar{v}$ (figure 9) gives no hint of the lack of vertical mixing in the bulk of the upper fluid layer. Instead, it has a well-mixed appearance.

Density profiles from the $u_* = 0.8$ cm s^{-1} case of the SR mode are shown in figure 10. They similarly indicate that despite the weak turbulence within the bulk of the upper layer, the latter is quite well mixed in density.

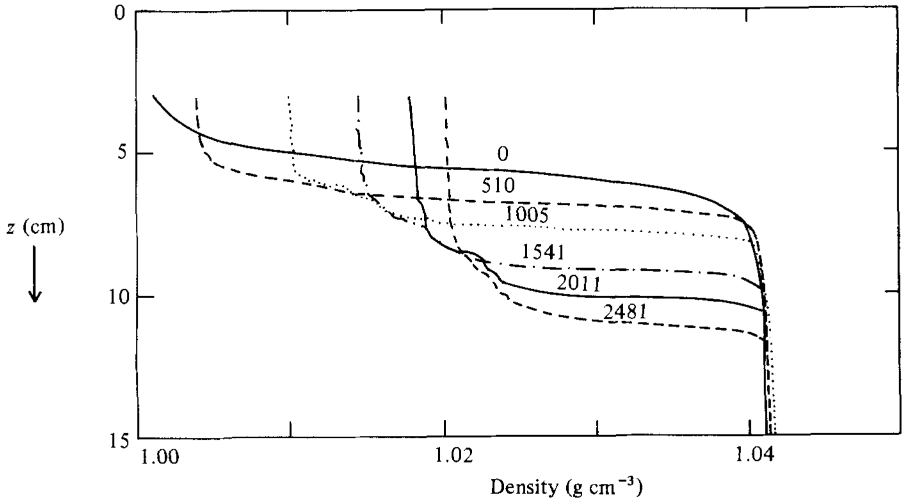

FIGURE 10. Density profiles for the SR mode labelled by the time in seconds after application of stress ($u_* = 0.8$ cm s^{-1}). Uppermost 3 cm of mixed layer were not probed.

3.5. *The Ekman layer and secondary circulation*

The shallow zone of turbulence just below the screen (figures 7 and 8) constitutes a turbulent Ekman layer, since within it there must be an approximate force balance between the radial pressure gradient, centrifugal force and vertical friction, as in the second equation of motion below:

$$\frac{\partial \bar{v}}{\partial t} \approx 0 \approx -\frac{\partial(\overline{v'w'})}{\partial z} - \frac{\bar{v}}{r}\bar{u}, \tag{7}$$

$$\frac{\partial \bar{u}}{\partial t} \approx 0 \approx -\frac{\partial(\overline{u'w'})}{\partial z} + \frac{\bar{v}}{r}\bar{v} - \bar{\rho}^{-1}\frac{\partial \bar{p}}{\partial r}, \tag{8}$$

where p is pressure. A slight tilt of the water surface at the screen edges, of opposite direction from that of the density interface, supplies the radial pressure gradient within (8) in the upper layer. A very rapid increase of the secondary circulation $\bar{u}$, a few millimetres below the screen, provides the turning of the mean velocity with depth. One difference from the classical atmospheric Ekman layer in a rotating frame, however, is that along a coordinate aligned in the direction of the surface shear stress, the annulus Ekman layer has no horizontal pressure gradient (see (7)). In the region of much weaker turbulence below the Ekman layer, the neglected radial- and vertical-advection and radial-stress terms become important in (7) and (8).

The picture we form from these observations is that of figure 11. The upper, less-dense layer is inferred to be rather well mixed in density and momentum, below the Ekman layer, only because of the secondary circulation, which carries mass and momentum out of the Ekman layer near the outer wall and distributes it throughout the rest of the upper layer. The Ekman layer is distinguished from the rest of the mixed layer not by any density contrast but by its much greater turbulence intensities and vertical shear-stress magnitude.† The deepening or growth of the Ekman depth with r sketched in the figure is inferred from the weak negative $\bar{u}$ at

---

† With this viewpoint the organized Reynolds stresses over the scale of the annulus, associated with the secondary circulation, are not regarded as turbulence.

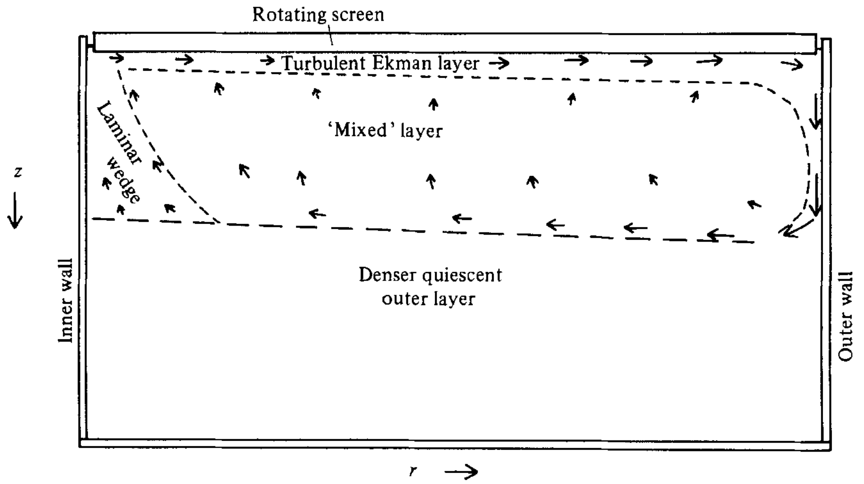

FIGURE 11. Schematic picture in the (r, z)-plane of the turbulent Ekman layer within the mixed layer, and the secondary circulation.

$z = 0.17\bar{h}$ of figure 3 near the inner wall, as well as from the consideration that the local Ekman layer is probably not in equilibrium and may entrain as it is carried towards the outer wall in the surface branch of the secondary circulation. The laminar wedge first observed by Scranton & Lindberg (1983) but not always evident in our experiments is also shown in figure 11. Turbulence at the outer wall that is carried towards $z = \bar{h}$ and then inwards is apparently damped strongly during its transit inwards.

This picture of annulus flow structure differs radically from that previously held (e.g. by Price 1979; Thompson 1979), in which the vertical frictional force tending to accelerate $\bar{v}$ had been thought to be balanced by sidewall drag (in the radial mean), throughout the bulk of the mixed layer. Instead, $\overline{v'w'}$ is non-existent in the bulk of the mixed layer of a typical annulus, and sidewall drag is balanced overall by advection of $\bar{v}$ carried by the secondary circulation. Almost all the sidewall drag is furthermore due to that at the outer wall (figure 6, $z/\bar{h} = 0.9$).

Although an increase of $\bar{v}$ would increase the Reynolds number within the interior of the mixed layer, obtaining turbulent flow throughout would require an order-of-magnitude deepening of the turbulent Ekman layer. Presumably this would require an order-of-magnitude increase of $0.4u_* r/\bar{v}$, which could be accomplished both by increasing r and by utilizing a rotating screen with roughened surface.

4. Inertial stability

Linear studies of inertial stability (e.g. Taylor 1923; Eliassen 1957) refer to the growth or damping of axisymmetric (circumferential) disturbances, but because of the fairly close analogy between rotating and stratified fluids (Veronis 1970) we expect the stability criterion to extend approximately to disturbances in general. However, in order to obtain an estimate of the importance of damping due to inertial stability in the presence of the opposing tendency due to vertical shear, the set of second-order turbulence equations in cylindrical coordinates was closed following Gibson & Rodi (1981) and solved numerically (see Appendix). Stringent assumptions include the

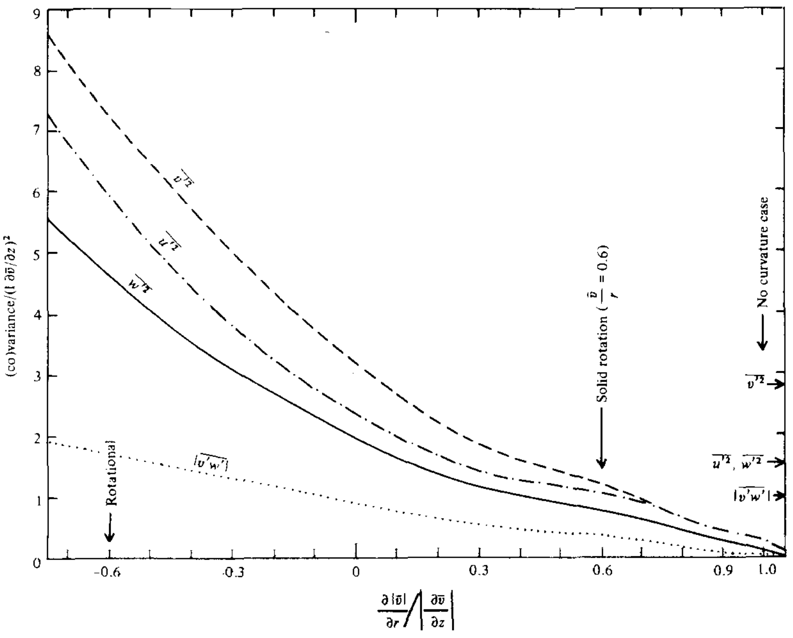

FIGURE 12. Normalized variances and covariance from a homogeneous turbulence model as a function of radial shear divided by vertical shear. Model values for zero curvature denoted by arrows on far right. An abscissa value of 0.6 corresponds to solid rotation, and −0.6 to irrotational flow.

neglect of triple-velocity correlations and mean advection by the secondary circulation.

One case treated was for $|\partial\bar{v}/\partial z| = \frac{5}{3}\partial|\bar{v}|/\partial r$, a vertical shear which can be seen from figures 9 and 6 to have been exceeded at depths less than about $0.15\bar{h}$. The resulting model dependencies of the turbulent (co)variances upon $(\partial|\bar{v}|/\partial r)/|\partial\bar{v}/\partial z|$ are shown in figure 12 for values of dimensionless radial shear ranging from irrotational to solid rotation and beyond. Results for the rectilinear case $r \to \infty$ are indicated at the right in the figure. Both the damping effect in approaching a state of solid rotation and enhancement in approaching a state of irrotationality are evident. Using the $\bar{v}$-profile of figure 6 for $z/\bar{h} = 0.17$, for which $\partial|\bar{v}|/\partial r$ equals or exceeds the value for solid rotation and $|\partial\bar{v}/\partial z|$ is much less or vanishingly small, the effect of inertial stability in damping the turbulence is predicted to be overwhelming. Figure 13 shows the model results for $|\partial\bar{v}/\partial z| = \frac{1}{3}|\bar{v}|/r$, or five times smaller than in the previous case. Turbulence intensities are then predicted to be reduced essentially to zero for $\partial|\bar{v}|/\partial r$ exceeding only about $\frac{1}{3}$ of the solid-rotation value. Although unrealistic oscillatory values of the turbulence intensities were obtained for values of the abscissa of 0.5 and greater, and realizability within the model then had to be enforced, the mean values of the variances for abscissae exceeding unity were negligible. Hence, if the mean vertical shear is large and the radial shear is small (i.e. close to the screen) the model predicts little effect of inertial stability, but within the bulk of the mixed layer where the shear distributions are reversed it predicts very strong damping. These results are consistent with our observations. It may also be noted that even for $\partial\bar{v}/\partial r = 0$, when the only shear is $\partial\bar{v}/\partial z$, the model yields $\overline{u'^2} > \overline{v'^2}$, in direct contrast with the case of no curvature. This inequality did not quite occur in the annulus, in comparing figures 4 and 5, suggesting that the model overemphasizes this effect of curvature.

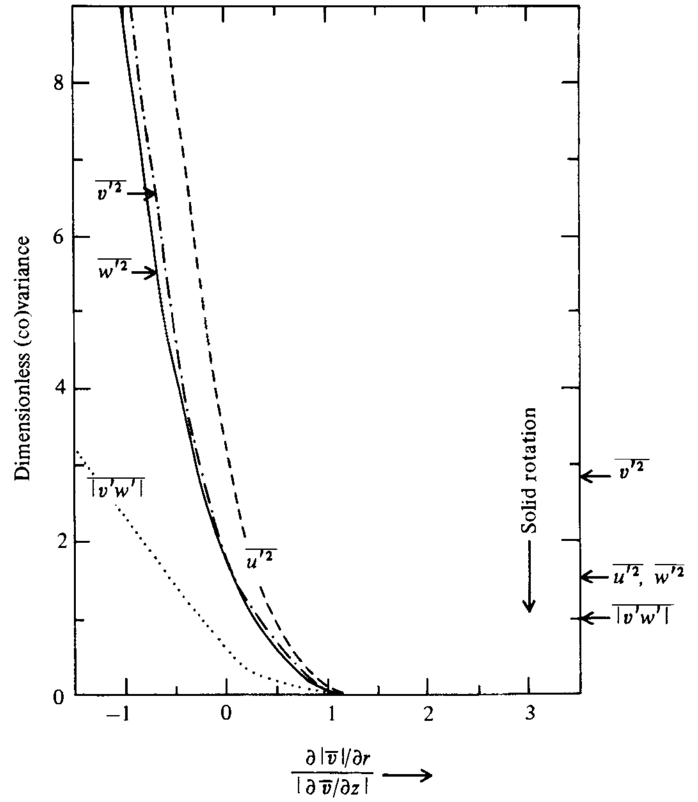

FIGURE 13. Normalized variances and covariance from the model as in figure 12, except for vertical shear five times smaller. Solid rotation corresponds to an abscissa value of 3.

5. The Couette-flow (CF) mode of stress input

In this mode, only the inner screen is present on top of the water surface; there is zero stress applied over the outer $\frac{2}{3}$ of the annulus surface area. The motivation is to provide a radial distribution of $r\bar{v}$ that more closely approximates irrotational flow than solid rotation. Since use of the inner screen alone may still tend to generate mean flow directly beneath which resembles solid rotation, roughness elements were added to its underside over its inner half from $r = 0.71$ m to $r = 0.75$ m. These consisted of 40 blocks, each $1 \times 1 \times 4.3$ cm, attached to the underside with the long axis along a radius, and spaced every 9°. These roughness elements were removed when utilizing the SR mode.

With this refinement, the radial profile of $r\bar{v}$ for the CF mode is shown in figure 6 for the case $u_* = 0.8$ cm s^{-1}. This u_* value again refers to the measured torque being distributed over the total annulus area and divided by the average radius. In this case the average depth of velocity measurement was $z = 0.5\bar{h}$. In comparing this profile against that of the SR mode for the greater depth, the angular momentum is much more uniform with radius. Due to the input of momentum near the inner wall, inertial stability is presumably absent except perhaps over the inner third of the annulus area.

The relative turbulence intensities $\overline{v'^2}/u_*^2$ and $\overline{w'^2}/u_*^2$ for the CF mode are presented in figures 14 and 15. Their magnitudes possess the values to be expected within a rectilinear boundary layer with uniformly applied stress decreasing uniformly with

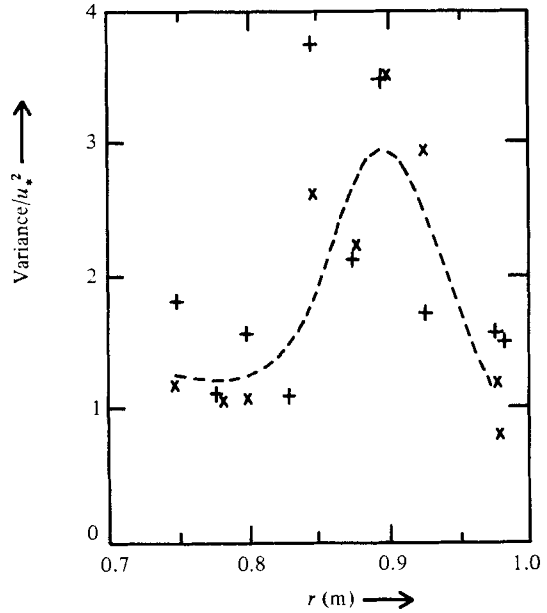

FIGURE 14. Radial profile of $\overline{v'^2}/u_*^2$ (+) and $\overline{u'^2}/u_*^2$ (×) for the CF mode for $z = 0.5\bar{h}$, $u_* = 0.8$ cm s^{-1}, and $\bar{h} = 8$–9 cm.

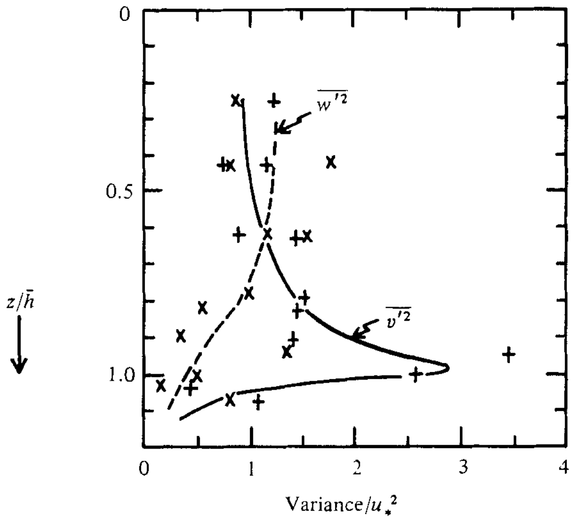

FIGURE 15. Scaled vertical profiles of $\overline{v'^2}/u_*^2$ (+, ——) and $\overline{w'^2}/u_*^2$ (×, – – – –) for the CF mode of operation. $u_* = 0.8$ cm s^{-1}, $\bar{h} = 8$–11 cm, $r = 0.85$ m.

depth to $z = \bar{h}$ (see e.g. Kundu 1980, figure 10). However, some enhancement due to inertial instability probably occurs. Also, a much stronger enhancement of $\overline{v'^2}$ occurs at the interface, due to interfacial shear concentrated there, than in Kundu's results. The much smaller turbulence intensities at the mixed-layer density interface with the SR mode than with the CF mode suggests that inertial stability also strongly damps the interfacial overturning otherwise associated with a moderately small gradient Richardson number at $z = \bar{h}$.

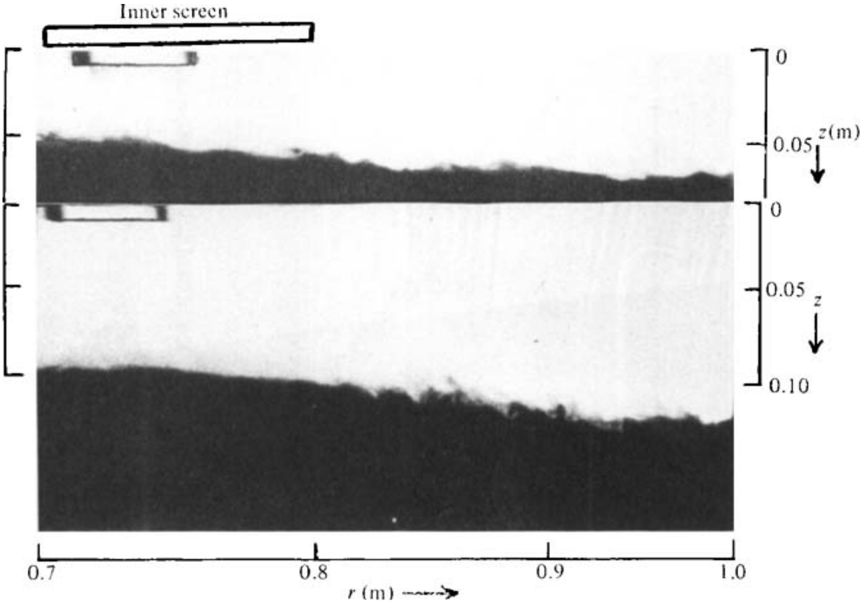

FIGURE 16. Vertical cross-sectional photograph of the mixed-layer density interface as in figure 2 but for the CF mode: (*a*) $\bar{h} = 7$ cm; (*b*) $\bar{h} = 11$ cm. $u_* = 0.8$ cm s^{-1}. In (*a*) interfacial irregularities occur throughout.

The structure of the interface in the CF mode is shown in the photographs of figure 16 for the same case of $u_* = 0.8$ cm s^{-1}. Turbulent cusps of entraining fluid that are sheared over appear to occur at all radii with roughly equal probability, for the shallower of the two depths shown. For the greater depth, however, stabilization underneath the inner screen sets in, thus indicating that even with this mode of operation $\bar{h}/W$ should be kept small (less than about 0.25).

The secondary circulation deduced for this CF mode from hot-film anemometer measurements consists of two counterrotating rolls with downward flow (away from the surface) centred where a peak in the turbulence intensities occurs (see figure 14). This circulation was confirmed by observing dye introduced from above at various radii and depths.

Density profiles for this case differed little from those of figure 10, except for exhibiting greater fluctuations near $z = \bar{h}$.

6. Entrainment rates with the CF mode

Since for $z/\bar{h}$ not too large the turbulence is relatively much more uniform with radius in the CF mode than in the SR mode, and occurs over the entire density interface, measurements of turbulent entrainment rate should be much more meaningful with the CF mode. When w_e from this mode was scaled with the u_* value obtained by distributing the screen torque over the entire annulus surface area, and was plotted against R_τ, values of w_e/u_* (see Yoon 1983) were found to lie in the vicinity of the curve of Kantha *et al.* (1977). (With the SR mode they lay a factor of 3–6 below this curve, intermediate to it and the even smaller values of Scranton & Lindberg (1983)). However, the results in this form cannot be simply interpreted, since only the inner 0.3 of the annulus surface had stress applied to it, and the

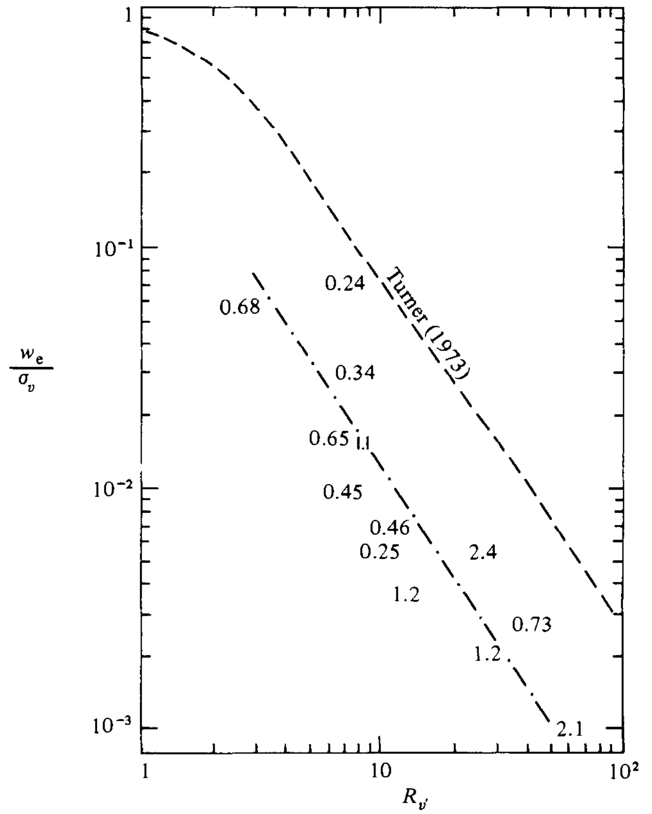

FIGURE 17. Entrainment scaled by σ_v at $z = \bar{h}$ versus $R_{v'} = (g/\bar{\rho})\Delta\rho\, l_v/\sigma_v^2$ from experiments using the CF mode. ----, Turner's (1973) experiments using salt. Numbers plotted are interfacial gradient Richardson numbers using differences across Δh.

distribution of $(\partial/\partial z)\overline{v'w'}$ within the annulus, and of other terms that maintained the turbulence, must have been very complex and radius dependent. Therefore a local turbulent scaling velocity $(\overline{v_h'^2})^{\frac{1}{2}} = \sigma_v$, is one possibility to be tested here, where subscript h refers to evaluation at $z = \bar{h}$. (It may be noted that at the radius at which $\overline{v'^2}$ was measured (0.85 m), its value lay very close to the average value over the annulus area; see figure 14). For a local lengthscale, the 'integral' lengthscale l_v for the circumferential velocity component along the circumferential s-coordinate at $z = \bar{h}$ will be tested. This constitutes Turner's (1973) entrainment-rate scaling which he applied to the case of oscillating-grid turbulence (Thompson & Turner 1975). Here l_v is defined as the spatial distance Δs (obtained from fixed-point measurements using Taylor's transformation $\Delta s = \bar{v}\,\Delta t$, where Δt is the time lag) at which the autocorrelation function drops to 1/e.

The normalized entrainment rate ω_e/σ_v was analysed as a function of the turbulence Richardson number $R_{v'}$, where

$$R_{v'} = \frac{g\,\Delta\rho}{\bar{\rho}}\frac{l_v}{\overline{v_h'^2}} \tag{9}$$

and $\overline{v_h'^2}$ was the average value at $r = 0.85$ m. Results of a series of measurements thus plotted are shown in figure 17 for the CF mode. Values of u_* ranged from 0.5 to

1.2 cm s^{-1}, though in any one experiment u_* was held constant. Values of $\bar{h}$ were centred at 7–8 cm, or about 0.25W. The plotted numbers are values of the bulk gradient interfacial Richardson number Ri_Δ given by

$$Ri_\Delta = \frac{g\,\Delta\rho}{\bar{\rho}}\frac{\Delta h}{(\Delta V)^2}, \tag{10}$$

where Δh is the estimated mean thickness of the interfacial zone across which about 95 % of the density jump $\Delta\rho$ occurs; ΔV is the velocity jump over the same interval. The dash–dot line through the data points is given by

$$w_e/\sigma_v = 0.38 R_v^{-1.5}. \tag{11}$$

Although the data points in figure 17 lie unexplainably below Turner's (1973) curve for salt by an average factor of about 6, there is little if any suggestion of a dependence on Ri_Δ, other than that which must exist because of the correlation between σ_v and ΔV. If confirmed, this would indicate that ΔV, though very important in determining the turbulence level at the interface, does not *directly* cause the entrainment; rather the interfacial turbulence resulting from shear and vertical transport drives the entrainment. Thus the interfacial shear is here inferred to be important in *indirectly* causing or enhancing the entrainment. It may be noted that values of the gradient Richardson number at the interface if based on maximum gradients of $\bar{\rho}$ and $\bar{v}$ existing at $z = \bar{h}$ would be somewhat smaller than the values of Ri_Δ presented.

Except in cases of very rapid entrainment (i.e. $w_e > 0.5$ mm s^{-1}) appreciable values of $\bar{v}$ and of $|\partial\bar{v}/\partial z|$ build up on the 'quiescent' side of the density interface within the annulus, as noted by Deardorff & Willis (1982), through mean viscous transfer and possibly gravity-wave momentum transport. Since no comparable transfer of density (salt) occurs, the outer fluid layer can eventually become weakly turbulent in the case of the two-layer system. This can cause weak entrainment by the outer layer of the mixed-layer fluid, producing a weak tail to the density distribution within the outer layer which should be excluded when estimating $\Delta\rho$, and more importantly, Δh and ΔV. This weak counter-entrainment constitutes detrainment when viewed from the more-active fluid, but was sufficiently weak here that the net entrainment observed (w_e) was considered to apply just to the active layer.

Another method for local scaling of the entrainment rate is to utilize for the velocity scale the vertical standard deviation $(\overline{w'^2_{hm}})^{\frac{1}{2}} = \sigma_w$, where subscripts hm refer to a height at the inner edge of the entrainment zone, taken here as $\bar{h}-\frac{1}{2}\Delta h$. Although $\overline{v'^2}$ has a maximum at a height very close to $z = \bar{h}$ (see figure 15) in the presence of significant interfacial shear, $\overline{w'^2}$ decreases rapidly as z exceeds z_{hm}, so that z_{hm} seems a more appropriate height of evaluation then $\bar{h}$. As an alternative lengthscale, Δh was chosen, although there is some question that a representative value can be obtained from individual density profiles. With this scaling, w_e/σ_w is presented as a function of R_w in figure 18, where

$$R_w = \frac{g\,\Delta\rho}{\bar{\rho}}\frac{\Delta h}{\sigma_w^2}. \tag{12}$$

The results agree fairly closely with a similar diagram due to Deardorff (1980) based on a three-dimensional numerical study of a cloud-capped mixed layer, upon taking $\Delta h = 0.1\bar{h}$ in that study and adjusting the evaluation of σ_w from $\bar{h}$ to $\bar{h}-\frac{1}{2}\Delta h$. The power-law portion of the dashed curve is given by

$$w_e/\sigma_w = 2.5 R_w^{-1.43} \tag{13}$$

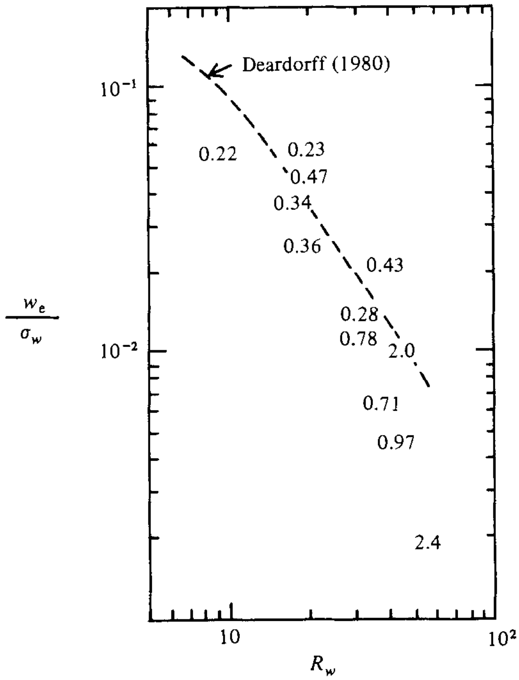

FIGURE 18. Entrainment rate scaled by σ_w at $z = \bar{h} - \frac{1}{2}\Delta h$ versus $R_w = (g/\bar{\rho})\, \Delta\rho\, \Delta h/\sigma_w^2$ from the same experiments as in figure 17 using the CF mode. Data points (labelled by gradient Richardson numbers) apply to somewhat later times in the experiments than those of figure 17.

For small values of w_e/σ_w the data suggest that the relationship ceases, possibly indicating that σ_w is then mostly associated with non-breaking internal waves which accomplish no entrainment.

It is not presently known which of these two local entrainment scalings is preferable, although the latter one may be if l_v is unavailable from theory or measurement. A possible explanation for the discrepancy between the data of figure 17 and Turner's (1973) curve is that $\overline{w'^2}$ may be more important than $\overline{v'^2}$ near $z = \bar{h}$ in relating the entrainment to the turbulence, and, owing to interfacial shear not present in his experiments, σ_v^2/σ_w^2 is substantially greater in the annulus than for oscillating-grid turbulence near $z = \bar{h}$. If this ratio were $6^{\frac{1}{3}} = 1.82$ times greater than in the oscillating-grid tank, holding other factors the same, the factor-of-6 discrepancy would be explained. Unfortunately, the radial variation of $\overline{v'^2}$ noted in figure 14 renders uncertain any such quantitative comparison.

7. Discussion and conclusions

Below a shallow turbulent Ekman layer adjacent to the rotating screen, mean angular momentum is found to increase strongly outwards (except very close to the outer wall). In this region of the mixed layer the turbulence is found to be very much weaker than would be expected if the vertical shear stress were distributed linearly with depth down to $z = \bar{h}$. These findings are consistent with the idea that inertial stability throughout the bulk of the 'mixed' layer acts powerfully to damp the turbulence. The turbulent entrainment rate, except very close to the annulus outer wall, is correspondingly reduced by the inertial stability. The annulus would need to be about an order of magnitude larger in diameter than the 2 m annulus used here in order that the Ekman layer occupy the whole of the mixed layer (of depth 5–10 cm) with inertial stability being minimal.

The fact that the conventional annulus produces w_e/u_* values as a function of R_τ which are apparently of the proper order of magnitude and which have proven useful in geophysical applications is here attributed to the following three factors.

(*a*) The ratio $\Delta V/u_*$ is often of similar magnitude in both the conventional annulus and the upper ocean mixed layer, especially during sudden onset of strong winds when flow speeds beneath the mixed layer are initially minimal. Therefore the important effect of ΔV upon entrainment (through its effect upon the interfacial turbulence) was roughly taken into account implicitly even though only u_* was accounted for explicitly.

(*b*) The laminar entrainment accomplished by the secondary circulation in the conventional annulus helps to compensate for the lack of turbulent entrainment over the inner half or more of the annulus.

(*c*) The strong turbulence very close to the annulus outer wall, where $\partial|\bar{v}|/\partial r$ does not support inertial stability, allows relatively rapid entrainment there, in partial compensation for the damping effect of inertial stability elsewhere.

Since the strength of the secondary circulation in the SR mode probably depends more on W than on $\bar{h}$, comment (*b*) above may explain why Jones & Mulhearn (1983) found W to be the appropriate lengthscale. The presence of secondary circulations in the annulus CF mode is not expected to affect w_e significantly since entrainment then occurs all along the (turbulent) density interface. It may also be noted that the presence of a secondary circulation, if of the proper scale and intensity, is probably desirable in simulation of the large eddies of this nature occurring in geophysical systems; e.g. longitudinal roll vortices (Brown 1970; Deardorff 1972; LeMone 1973) or Langmuir circulations (Faller 1971).

Upon utilizing a Couette-flow (CF) mode of operation of the annulus, it is shown that the mean flow in the mixed layer becomes closer to irrotational across the bulk of the annulus area. The turbulence level and irregularity of the density interface are then found to be relatively more uniform with radius, with turbulent entrainment occurring rather uniformly over the entire density interface except close to the inner wall where inertial stability can still prevail if $\bar{h}$ is too large.

It is concluded that the CF mode of operation of the (modified) annulus is a valid method of investigating mixed-layer entrainment in the presence of interfacial shear, provided that local scaling is used in both the dimensionless entrainment rate and the Richardson number involved. The turbulent circumferential velocity component at the density interface is then used as the velocity scale and an integral lengthscale for this component as the scaling length. As an alternative, the root-mean-square vertical-velocity component and the mean thickness of the entrainment zone were also tested as the velocity and lengthscales. In either case the dimensionless entrainment rate appears to have little if any explicit dependence upon interfacial velocity shear using the local turbulence scaling, although the circumferential turbulence component is much enhanced by the interfacial shear (figure 15). However, with this method of scaling the entrainment, the problem remains of how to relate the internal velocity and length scales to better known scales associated with external forcing. The use of only local entrainment scaling thus cannot address this more practical problem, but could be of value for theoretical studies in which the second-moment variance and covariance equations involving entrainment terms are closed at $z = \bar{h}$.

This research was supported by the Office of Naval Research, and by the National Science Foundation, Division of Atmospheric Sciences, under Grant ATM 8019778. The dedicated efforts of G. E. Willis in preparing for the experiments, including calibrations of the conductivity probe, stress–strain gauges and traversing mechanisms, and his conduction of the experiments, including photography of the interface, are greatly appreciated. The technical expertise of P. Stockton in all phases of the experimental work and data collection was also indispensable. We thank P. Katen for the use of his graphical-plotting device. Comments from G. E. Willis, W. R. Lindberg and L. Mahrt were very helpful in writing the manuscript.

Appendix. The second-moment model

Let $u_1 = u$ (the radial or r velocity component), $u_2 = v$ (azimuthal or circumferential component) and $u_3 = w$ (the vertical, z-component). We shall non-dimensionalize the second-moment turbulence rate equations using as lengthscale l (a vertical mixing length), as timescale $\partial\bar{v}/\partial z$, and as velocity scale $l\,\partial\bar{v}/\partial z$. Upon neglecting $\bar{u}$, $\bar{w}$ and triple-fluctuation products, the predictive equations for the dimensionless second-moment velocity correlations (using dimensional notation) in cylindrical coordinates are then

$$\frac{\partial}{\partial t}\overline{u_i'u_j'} = (1-c_2)\,P_{ij}+\tfrac{2}{3}c_2\delta_{ij}P-c_3q(\overline{u_i'u_j'}-\tfrac{1}{3}\delta_{ij}q^2)-\tfrac{2}{3}\delta_{ij}\epsilon, \tag{A 1}$$

where δ_{ij} is the Kronecker delta, and

$$q = (\overline{u'^2}+\overline{v'^2}+\overline{w'^2})^{\frac{1}{2}},$$

$$P_{11} = 4\frac{\bar{v}}{r}\overline{u'v'}, \tag{A 2}$$

$$P_{22} = -2\overline{u'v'}\left(\frac{\partial\bar{v}}{\partial r}+\frac{\bar{v}}{r}\right)-2\overline{v'w'}\frac{\partial\bar{v}}{\partial z}, \tag{A 3}$$

$$P_{33} = 0, \tag{A 4}$$

$$P_{12} = 2\frac{\bar{v}}{r}(\overline{v'^2}-\overline{u'^2})-\overline{u'^2}\left(\frac{\partial\bar{v}}{\partial r}-\frac{\bar{v}}{r}\right)-\overline{u'w'}\frac{\partial\bar{v}}{\partial z}, \tag{A 5}$$

$$P_{23} = -\overline{w'^2}\frac{\partial\bar{v}}{\partial z}-\overline{u'w'}\left(\frac{\partial\bar{v}}{\partial r}+\frac{\bar{v}}{r}\right), \tag{A 6}$$

$$P_{13} = 2\frac{\bar{v}}{r}\overline{v'w'}, \tag{A 7}$$

$$P = \tfrac{1}{2}(P_{11}+P_{22}+P_{33}), \tag{A 8}$$

$$\epsilon = c'q^3, \tag{A 9}$$

$$c_1 = 1.8, \quad c_2 = 0.6, \quad c' = 0.06992, \quad c_3 = 2c_1c'. \tag{A 10}$$

The closure assumptions and values of c_1 and c_2 are from the study of Gibson & Rodi (1981), except that instead of utilizing a prediction equation for the dimensionless dissipation rate ϵ it is closed in the usual manner of (A 9). The particular choice of c' in (A 10) allows $(l\,\partial\bar{v}/\partial z)^2$ to be equivalent to $|\overline{v'w'}|$ in the absence of curvature.

These equations are most applicable toward the study of fully three-dimensional turbulence (not just axisymmetric turbulence) because the P_{ij} terms redistribute kinetic energy as is idealized for three-dimensional turbulence.

For abscissa values in figure 12 in excess of about 0.3, the final state reached was oscillatory with a period of 7–10 $|\partial v/\partial z|^{-1}$. For abscissa values in excess of about 0.6 the out-of-phase oscillations in the variances $\overline{u'^2}$ and $\overline{v'^2}$ were such as to require that realizability be enforced.

REFERENCES

BROWN, R. A. 1970 A secondary flow model for the planetary boundary layer. *J. Atmos. Sci.* **27**, 742–757.

COMTE-BELLOT, G. 1965 Écoulement turbulent entre deux parois parallèles. *Publ. Sci. Tech. Min. de l'Air*, no. 419.

DEARDORFF, J. W. 1972 Numerical investigation of neutral and unstable planetary boundary layers. *J. Atmos. Sci.* **29**, 91–115.

DEARDORFF, J. W. 1980 Stratocumulus-capped mixed layers derived from a three-dimensional model. *Boundary-Layer Met.* **18**, 495–527.

DEARDORFF, J. W. & WILLIS, G. E. 1982 Dependence of mixed-layer entrainment on shear stress and velocity jump. *J. Fluid Mech.* **115**, 123–149.

DENMAN, K. L. & MIYAKE, M. 1973 Upper layer modification of ocean station Papa: observations and simulation. *J. Phys. Oceanog.* **3**, 185–196.

ELIASSEN, A. 1957 Dynamic meteorology. In *Handbuch der Physik*, Band **48**, *Geophysik* II (ed. S. Flugge). Springer.

ELLISON, T. H. & TURNER, J. S. 1959 Turbulent entrainment in stratified flows. *J. Fluid Mech.* **6**, 423–448.

FALLER, A. J. 1971 Oceanic turbulence and the Langmuir circulations. *Ann. Rev. Ecol. & Syst.* **2**, 201–236.

GIBSON, M. M. & RODI, W. 1981 A Reynolds-stress closure model of turbulence applied to the calculation of a highly curved mixing layer. *J. Fluid Mech.* **103**, 161–182.

JONES, I. S. F. & MULHEARN, P. J. 1983 The influence of external turbulence on sheared interfaces. *Geophys. Astrophys. Fluid Dyn.* **24**, 49–62.

KANTHA, L. H. 1978 On surface-stress induced entrainment at a buoyancy interface. *The Johns Hopkins Univ. GFDL TR* 78–1.

KANTHA, L. H., PHILLIPS, O. M. & AZAD, R. S. 1977 On turbulent entrainment at a stable density interface. *J. Fluid Mech.* **79**, 753–768.

KATO, H. & PHILLIPS, O. M. 1969 On the penetration of a turbulent layer into stratified fluid. *J. Fluid Mech.* **37**, 643–655.

KUNDU, P. K. 1980 A numerical investigation of mixed-layer dynamics. *J. Phys. Oceanogr.* **10**, 220–236.

LEMONE, M. A. 1973 The structure and dynamics of horizontal roll vortices in the planetary boundary layer. *J. Atmos. Sci.* **30**, 1077–1091.

LOFQUIST, K. 1960 Flow and stress near an interface between stratified fluids. *Phys. Fluids* **3**, 158–175.

LUMLEY, J. L. & PANOFSKY, H. A. 1964 *The Structure of Atmospheric Turbulence.* Interscience.

MOORE, M. J. & LONG, R. R. 1971 An experimental investigation of turbulent stratified shearing flow. *J. Fluid Mech.* **49**, 635–655.

NIILER, P. P. & KRAUS, E. B. 1977 One-dimensional models of the upper ocean. In *Modelling and Prediction of the Upper Layers of the Ocean* (ed. E. B. Kraus), pp. 143–172. Pergamon.

PRICE, J. F. 1979 On the scaling of stress-driven entrainment experiments. *J. Fluid Mech.* **90**, 509–529.

SCRANTON, D. R. & LINDBERG, W. R. 1983 An experimental study of entraining, stress-driven, stratified flow in an annulus. *Phys. Fluids* **26**, 1198–1205.

TAYLOR, G. I. 1923 Stability of a viscous liquid contained between two rotating cylinders. *Phil. Trans. R. Soc. Lond.* A **223**, 289–343.

THOMPSON, R. O. R. Y. 1979 A re-examination of the entrainment process in some laboratory flows. *Dyn. Atmos. Oceans* **4**, 45–55.

THOMPSON, S. M. & TURNER, J. S. 1975 Mixing across an interface due to turbulence generated by a grid. *J. Fluid Mech.* **67**, 349–368.

TURNER, J. S. 1973 *Buoyancy Effects in Fluids.* Cambridge University Press.

VERONIS, G. 1970 The analogy between rotating and stratified fluids. *Ann. Rev. Fluid Mech.* **2**, 37–66.

YOON, S.-C. 1983 The structure of turbulent entraining flow in an annulus with a rotating screen. Ph.D. thesis, Dept Atmos. Sci., Oregon State Univ., Corvallis.